Stopping dynamics of ions passing through correlated honeycomb clusters

Karsten Balzer,[1,*] Niclas Schlünzen,[2] and Michael Bonitz[2]

[1]*Rechenzentrum, Christian-Albrechts-Universität zu Kiel, Ludewig-Meyn-Strasse 4, 24118 Kiel, Germany*

[2]*Institut für Theoretische Physik und Astrophysik, Christian-Albrechts-Universität zu Kiel, Leibnizstrasse 15, 24098 Kiel, Germany*

A combined nonequilibrium Green functions–Ehrenfest dynamics approach is developed that allows for a time-dependent study of the energy loss of a charged particle penetrating a strongly correlated system at zero and finite temperatures. Numerical results are presented for finite inhomogeneous two-dimensional Fermi-Hubbard models, where the many-electron dynamics in the target are treated fully quantum mechanically and the motion of the projectile is treated classically. The simulations are based on the solution of the two-time Dyson (Keldysh-Kadanoff-Baym) equations using the second-order Born, third-order, and T-matrix approximations of the self-energy. As application, we consider protons and helium nuclei with a kinetic energy between 1 and 500 keV/u passing through planar fragments of the two-dimensional honeycomb lattice and, in particular, examine the influence of electron-electron correlations on the energy exchange between projectile and electron system. We investigate the time dependence of the projectile's kinetic energy (stopping power), the electron density, the double occupancy, and the photoemission spectrum. Finally, we show that, for a suitable choice of the Hubbard model parameters, the results for the stopping power are in fair agreement with *ab initio* simulations for particle irradiation of single-layer graphene.

I. INTRODUCTION

The interaction of particles with matter is a fundamental aspect of physics and allows one to measure their properties in colliding-beam or beam-target experiments. Conversely, the irradiation of matter by particles can be used also as a diagnostic tool to probe the static and dynamic properties of matter itself. In soft collisions of heavy charged particles, such as ions, with a solid, typically the electrostatic force, i.e., the Coulomb interaction, has the largest impact, leading to excitation and ionization of electrons in the target material and thus to the loss of kinetic energy of the projectile [1]. For nonrelativistic projectile velocities of the order of or larger than the Fermi velocity ($\sim 10^6$ m/s in metals), theoretical approaches based on scattering theory [2] or on the response functions of the homogeneous electron gas [3], can give a quantitative description of the energy transferred during the collision process but neglect the precise atomic composition of the target.

Regarding first-principles modeling in the same velocity regime, recent theoretical progress is due to time-dependent density functional theory (TDDFT), which has been applied to describe the slowing down of charged particles in a variety of solids, including metals [4–6], semimetals [7,8] and clusters [9,10], narrow-band-gap semiconductors [11], and insulators [12,13]. Taking into account primarily the excitation of valence electrons, these simulations yield satisfactory results for the electronic stopping power (the transfer of energy to the electronic degrees of freedom per unit length traveled by the projectile) and work for a wide range of impact energies. On the other hand, one can quite generally determine the stopping power of energetic ions in matter using the SRIM code [14], which uses the binary collision approximation in combination with an averaging over a large range of experimental situations

to provide energy loss and range tables for many materials and gaseous targets. In principle, TDDFT and SRIM can include effects of electron-electron correlations on the stopping behavior, either by using exchange-correlation potentials beyond the local density approximation in TDDFT, e.g., [15,16], or by including static exchange and correlation contributions to the interaction energy between overlapping electron shells in SRIM. Despite these capabilities, both methods have, however, difficulties to approach *strong* Coulomb correlations, which are crucial, e.g., in transition-metal oxides [17] or specific organic materials [18]. In addition, we note that SRIM does account neither for the exact crystal structure of the material nor dynamic (i.e., time-dependent) changes in the target during the collision process, which limits its applicability.

It is, therefore, interesting to consider an alternative approach to the stopping power that does not have these limitations: nonequilibrium Green functions (NEGF) [19,20]. This method allows one to systematically include electron-electron correlations via a time-dependent many-body self-energy, and it has recently successfully been applied to strongly correlated lattice systems as well [21]. Particular advantages of the NEGF approach are that it is not limited to either weak or strong coupling and that it is particularly well suited to study finite-sized clusters and spatially inhomogeneous systems on a self-consistent footing. While the NEGF approach is computationally very demanding, in recent years efficient numerical schemes have been developed to solve the underlying Keldysh-Kadanoff-Baym equations (KBE) [22–29].

Here, we extend the NEGF approach by including the interaction with a classical projectile using an Ehrenfest-type approach that is well established in TDDFT simulations. Our goal is to develop a full time-dependent and space-resolved description, which is necessary as the projectile induces local time-dependent changes to the electron density and to the local band structure. This allows us, in particular, to consider finite clusters of size L, which are of substantial current interest. Furthermore, we study the size dependence of the response

---

*balzer@rz.uni-kiel.de

to the projectile. At the same time, the thermodynamic limit of the stopping power (cluster size L approaching infinity) is more difficult and expansive to obtain, as it requires an extrapolation of results for different L. Nevertheless, we obtain good agreement with existing results for macroscopic systems.

To implement this approach, we choose, as a first application, the energy deposition of simple ions (protons and alpha particles), where there is no interatomic electron dynamics, in planar two-dimensional honeycomb clusters, in which the electron dynamics is well described in terms of a Fermi-Hubbard model. To investigate the importance of electronic correlation effects, we vary the coupling strength from small to moderate values (up to $U/J = 4$) and test various self-energy approximations, such as the second Born and the much more involved T-matrix approximation. The results are compared to mean-field (Hartree) results, which are provided by the same NEGF program.

The paper is organized as follows. In Sec. II, we define the model Hamiltonian, discuss the interaction potential between projectile and target, and describe the self-consistent computational scheme, which allows us to calculate the correlated electron dynamics on the honeycomb clusters. In Sec. III, we review the equilibrium properties of the target system, which are sensitive to correlations, and then present the main results for the stopping dynamics in Sec. IV. Here, we primarily focus on the effect of electron-electron correlations on the energy transfer, analyze the time-dependent collision process for a wide range of projectile velocities, and consider different initial states and temperatures. In Sec. V, we finally discuss the application of the used model to graphene and conclude the paper with Sec. VI, outlining possible future work.

II. COMPUTATIONAL SETUP

A. Model

To study the stopping dynamics of a classical charged particle which passes through a (strongly) correlated system, we consider a finite lattice of electrons described by a single-band Fermi-Hubbard model and monitor the transfer of energy during the collision process. Taken as a whole, the lattice system is electrically neutral, i.e., the electronic charges are compensated by corresponding opposite charges located at the site coordinates $\mathbf{R}_i$. The general stopping mechanism is mediated by the bare Coulomb interaction between the projectile, the fixed background charges, and the target electrons which are initially in equilibrium. Throughout, we focus on positively charged ions as projectiles, which, when approaching the lattice, induce a confinement potential to the electrons and thus initiate a nonequilibrium electron dynamics. In turn, the ions (of mass m_p and charge $Z_\mathrm{p}e$) react to any charge redistribution on the lattice and change their position and kinetic energy accordingly.

As lattice systems, we choose circular honeycomb clusters, which are oriented in the xy plane and have a finite number of honeycombs, yielding in total L sites (see Fig. 1 for an illustration). We consider a half-filled system in the paramagnetic phase and, to generate realistic results, set the lattice spacing to $a_0 = 1.42$ Å, which corresponds to the carbon-carbon bond length in graphene [30]. Using a nearest-neighbor hopping J
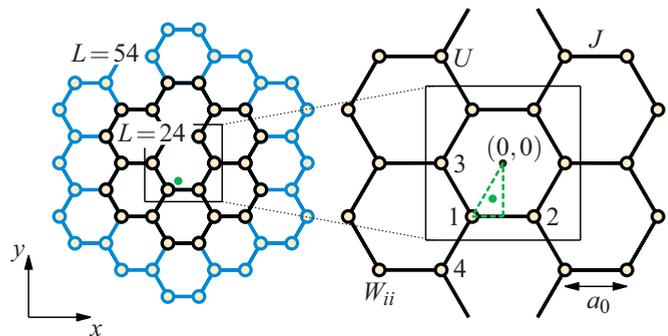
FIG. 1. Lattice structure of circular honeycomb clusters with $L = 24$ (black) and 54 sites (blue). The green point indicates the position where the projectile hits the lattice plain. For further reference, we label four sites in the center of the clusters, where we will monitor the time-dependent electron density in Sec. IV B. Furthermore, a_0 denotes the lattice spacing, J (U) is the nearest-neighbor hopping (the onsite interaction), and W_{ii} is the local energy defined in Eq. (2).

and an onsite Coulomb repulsion U, the Hamiltonian for the lattice electrons is then given by

$$H_\mathrm{e}(t) = -J \sum_{\langle i,j \rangle, \sigma} c_{i\sigma}^\dagger c_{j\sigma} + U \sum_i \left(n_{i\uparrow} - \frac{1}{2} \right)\left(n_{i\downarrow} - \frac{1}{2} \right)$$
$$+ \sum_{ij,\sigma} W_{ij}(t) c_{i\sigma}^\dagger c_{j\sigma}, \tag{1}$$

where the operator $c_{i\sigma}^\dagger$ ($c_{i\sigma}$) creates (annihilates) an electron with spin σ on site i, $n_{i\sigma} = c_{i\sigma}^\dagger c_{i\sigma}$ denotes the electron density, and W_{ij} are the matrix elements of the confinement potential induced by the projectile. In Sec. IV, we imply localized electronic wave functions $\varphi_i(\mathbf{r}) \propto \delta(\mathbf{r} - \mathbf{R}_i)$, for which we can resort to the diagonal components of this potential:

$$W_{ii}(t) = -\frac{e^2}{4\pi\epsilon_0} \frac{Z_\mathrm{p}}{|\mathbf{r}_\mathrm{p}(t) - \mathbf{R}_i|}, \tag{2}$$

where $\mathbf{r}_\mathrm{p}(t)$ denotes the time-dependent position of the projectile, $-e$ is the electron charge, and ϵ_0 the vacuum permittivity. Moreover, in Sec. V, we improve this model by including also terms $W_{ij}(t)$ with $|i - j| = 1$, which locally renormalize the nearest-neighbor hopping [cf. Eq. (14)].

For convenience, we measure J and U in electron volts, define U/J as the interaction strength for the electrons, and use $t_0 = \hbar/J$ as the unit of time. Unless otherwise stated, we use $J = 2.8$ eV (which is typical for graphene [31]) to fix the time scale.

B. Computational method

To compute the classical motion of the projectile with an initial velocity $d\mathbf{r}_\mathrm{p}/dt = (0,0,v_z)$, we solve Newton's equation with the total potential

$$V(\mathbf{r}_\mathrm{p},t) = \frac{e^2}{4\pi\epsilon_0} \sum_i \frac{Z_\mathrm{p} Z_i(t)}{|\mathbf{r}_\mathrm{p}(t) - \mathbf{R}_i|} \tag{3}$$

created by all lattice charges [here, $Z_i(t) = 1 - \sum_\sigma \langle n_{i\sigma} \rangle(t)$ denotes the net charge on the lattice site i]. For the solution we

use a three-dimensional velocity-Verlet algorithm. Motivated by TDDFT calculations [7], we set the initial position of the incident ion to $\mathbf{r}_\mathrm{p} = (-\frac{1}{6}a_0, -\frac{\sqrt{3}}{3}a_0, -z)$ (see the centroid point of the green dashed triangle in Fig. 1). These coordinates have been found to give similar stopping results for the highly symmetric honeycomb lattice compared to calculations, where one averages over many different collision sites. This allows us to avoid averaging over many trajectories and to directly compare to previous TDDFT results (Sec. V). Furthermore, the initial z position is chosen such that the measured energy transfer becomes independent of the initial conditions (typically $z \gtrsim 10a_0$).

To compute the correlated time evolution of the lattice electrons, we use a quantum statistical approach based on the one-particle nonequilibrium Green function (NEGF)

$$G_{ij\sigma}(t,t') = -\frac{\mathrm{i}}{\hbar}\langle T_\mathcal{C} c_{i\sigma}(t) c_{j\sigma}^\dagger(t')\rangle, \qquad (4)$$

which is defined on the Keldysh time contour $\mathcal{C}$ [32] and can be interpreted as a two-time generalization of the one-particle density matrix

$$\langle \rho_{ij\sigma}\rangle(t) = \langle c_{i\sigma}^\dagger c_{j\sigma}\rangle = -\mathrm{i}\hbar\, G_{ji\sigma}(t,t^+). \qquad (5)$$

On the contour, $T_\mathcal{C}$ furthermore denotes the time-ordering operator, $\langle T_\mathcal{C} \ldots\rangle = \mathrm{tr}[T_\mathcal{C}\exp(S)\ldots]/\mathrm{tr}[T_\mathcal{C}\exp(S)]$ with $S = -\mathrm{i}/\hbar \int_\mathcal{C} ds\, H_\mathrm{e}(s)$ defines the ensemble average, and the notation t^+ means that the time t^+ is infinitesimally larger along $\mathcal{C}$ than t. The equations of motion of the greater and less components of the NEGF (4),

$$\begin{aligned}
G_{ij\sigma}^>(t,t') &= -\frac{\mathrm{i}}{\hbar}\langle c_{i\sigma}(t) c_{j\sigma}^\dagger(t')\rangle, \\
G_{ij\sigma}^<(t,t') &= \frac{\mathrm{i}}{\hbar}\langle c_{j\sigma}^\dagger(t') c_{i\sigma}(t)\rangle,
\end{aligned} \qquad (6)$$

follow from the time evolution of the creation and annihilation operators in the Heisenberg representation and are known as the two-time Keldysh-Kadanoff-Baym equation (KBE) [19,20,23]:

$$\begin{aligned}
\sum_k [\mathrm{i}\hbar\,\partial_t \delta_{ik} &- h_{ik\sigma}(t)] G_{kj\sigma}^{\gtrless}(t,t') \\
&= \delta_\mathcal{C}(t,t')\delta_{ij} + \sum_k \left\{ \int_\mathcal{C} ds\, \Sigma_{ik\sigma}(t,s) G_{kj\sigma}(s,t') \right\}^{\gtrless}. \qquad (7)
\end{aligned}$$

Here, $\delta_\mathcal{C}$ denotes the delta function on the contour, and $h_{ij\sigma}(t)$ is the time-dependent effective one-particle Hamiltonian, which explicitly includes the Hartree contribution to the electron-electron interaction, i.e.,

$$h_{ij\sigma}(t) = \underbrace{-J\delta_{\langle i,j\rangle}}_{=J_{ij}} + \left\{ W_{ii}(t) + U\left[\langle n_{i\bar\sigma}\rangle(t) - \tfrac{1}{2}\right]\right\}\delta_{ij}, \qquad (8)$$

with the density $\langle n_{i\sigma}\rangle(t) = -\mathrm{i}\hbar G_{ii\sigma}^<(t,t)$. On the right-hand side of Eq. (7), the contour integral defines the memory kernel of the KBE, in which $\Sigma_{ij\sigma}(t,t')$ denotes the correlation part of the self-energy [i.e., the mean-field part is excluded as it is contained in Eq. (8)]. Systematic expressions for the self-energy can be constructed by many-body perturbation theory, e.g., using diagram techniques [20,33]. Below, we treat the

correlation self-energy Σ in different approximations, which conserve particle number, momentum, and energy.

C. Many-body approximations

We consider the correlation self-energy Σ in the following approximations:

(1) As the simplest self-energy beyond the (Hartree) mean-field level, we consider the second-order Born approximation (2B),

$$\Sigma_{ij\sigma}^{\mathrm{2B},\gtrless}(t,t') = \hbar^2 U^2 G_{ji\sigma}^{\gtrless}(t,t') G_{ji\bar\sigma}^{\gtrless}(t,t') G_{ij\bar\sigma}^{\lessgtr}(t',t), \qquad (9)$$

which includes all irreducible diagrams of second order in the interaction U. Aside from the full evaluation of this self-energy, we will consider, in addition, the *local* (in space) second Born approximation, which includes only the diagonal components $\Sigma_{ii\sigma}^{\mathrm{2B}}$ of the self-energy (9). This approximation substantially reduces the numerical complexity, as it allows to solve the KBE via particularly efficient schemes [34–36]. We note that the 2B approximation is a perturbation theory result and, therefore, becomes less accurate when U increases.

(2) We consider the particle-particle T-matrix (TM) self-energy, which sums up the whole Born series including diagrams of all orders in U and is given by [37]

$$\Sigma_{ij\sigma}^{\mathrm{TM}}(t,t') = \mathrm{i}\hbar\, T_{ij}(t,t') G_{ji\bar\sigma}(t',t), \qquad (10)$$

with the effective interaction

$$\begin{aligned}
T_{ij}(t,t') &= -\mathrm{i}\hbar\, U^2 G_{ij\sigma}(t,t') G_{ij\bar\sigma}(t,t') \\
&\quad + \mathrm{i}\hbar\, U \sum_k \int_\mathcal{C} ds\, G_{ik\sigma}(t,s) G_{ik\bar\sigma}(t,s) T_{kj}(s,t').
\end{aligned}$$

The T-matrix approximation has been found to perform very well in the regime of small (or large) density, i.e., away from half-filling [33,37,38]. If the number of electrons and holes become comparable, however, particle-hole interaction processes gain in importance, which are not captured by the particle-particle T-matrix.

(3) In order to accurately treat strongly correlated systems, we also consider the third-order approximation [38], which exactly takes into account all self-energy contributions up to $\mathcal{O}(U^3)$. This approximation has been found advantageous around half-filling, in particular, for small to moderate interaction strengths [38].

(4) We also consider the generalized Kadanoff-Baym ansatz (GKBA) of Lipavský *et al.* [39], which has recently attracted growing attention [28,29,33,40]. By reconstructing the two-time Green function $G_{ij\sigma}(t,t')$ from its time-diagonal value, the GKBA provides a way to substantially reduce the numerical effort of the computation of the NEGF, while still accurately accounting for particle number and energy conservation and correlations. Here, we will apply the GKBA to the second-order Born self-energy using mean-field type propagators (HF-GKBA) (for details see Refs. [29,33]). This allows us to increase the simulation duration and extend the calculations to lower projectile energies (see Sec. IV D).

With these self-energies, the KBE (7) is solved together with its adjoint equation by a self-consistent time propagation scheme in the two-time plane, starting from a given initial-state Green function at $t,t' = 0$. For details on the numerical

solution of the two-time KBE including the above approximations, we refer the reader to Refs. [23,25,27,33]. To investigate the influence of the initial state of the many-electron system on the dynamics and the energy loss of the projectile, we consider two relevant cases. For the example of the system being initially in the ground state (we set $k_B T = \beta^{-1} = 0.01$ eV and note that the case of finite temperature is discussed separately in Sec. IV E), we consider the following:

(A) The stationary correlated equilibrium state, which is formed via a relaxation that starts in the Hartree ground state (see Sec. III for details). This is, of course, only an approximation to the true ground state but it substantially reduces the computation time.

(B) The fully correlated ground state. It is obtained via a time-dependent procedure (adiabatic switch-on of the interaction U) (see, e.g., Refs. [33,41] for details).

For the case of half-filling (chemical potential $\mu = 0$), the Hartree ground state of Hamiltonian (1) (with $W_{ij} \equiv 0$) is independent of U and is given by the density matrix

$$\langle \rho_{ij\sigma} \rangle (t = 0) = -i\hbar\, G^<_{ji\sigma}(0,0)$$

$$= -i\hbar \sum_k v^*_{ki} v_{kj} f_\beta(\epsilon_k, \mu), \quad (11)$$

where ϵ_k ($\mathbf{v}_k$) are the eigenvalues (eigenvectors) of the hopping matrix $(\mathbf{J})_{ij} = J\delta_{\langle i,j\rangle}$, and $f_\beta(\epsilon, \mu) = 1/(e^{\beta(\epsilon-\mu)} + 1)$ is the Fermi-Dirac distribution.

III. LATTICE PROPERTIES PRIOR TO THE IMPACT

In this section, we solve the KBE (7) without the incident projectile and compute central equilibrium properties of the honeycomb clusters primarily in the local second Born approximation. First, we analyze the double occupations

$$\langle d_i \rangle = \langle n_{i\uparrow} n_{i\downarrow} \rangle = -\frac{i\hbar}{U} \sum_k \int_\mathcal{C} ds\, \Sigma_{ik\sigma}(t,s) G_{ki\sigma}(s,t^+) \quad (12)$$

on the lattice sites i, which contain important information about the correlations in the system.

In Fig. 2, we show results for the average double occupation $\langle d \rangle_{av} = \frac{1}{L} \sum_i \langle n_{i\uparrow} n_{i\downarrow} \rangle$ on clusters of different size L, which is established over time, when the system is prepared in the Hartree ground state [Eq. (11), case (A)]. We find that the emerging double occupation is practically independent of the system size, which is even the case for larger values of the interaction strength. The value $\langle d \rangle_{av}$ is, up to $U/J \lesssim 4$, in reasonable agreement with exact quantum Monte Carlo data (black triangles) for the extended honeycomb lattice [42]. The right panel of Fig. 2 gives details on the time dependence of the double occupation during this (fictitious) relaxation. Clearly, the sudden switch-on of the correlation part of the self-energy at $t = 0$ leads to an oscillatory transient response, after which the double occupation rapidly reaches a new (correlated) stationary value. The site densities ($\langle n_{i\sigma} \rangle = 0.5$) remain constant during this relaxation because we consider an undoped system with particle-hole symmetry. We note that this final state is a stationary correlated state, which slightly differs from the correlated ground state as it has a slightly larger total energy (due to correlation-induced heating [43,44]) (cf. the
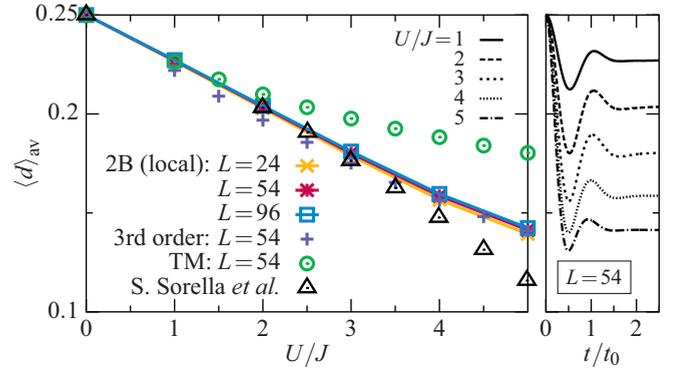
FIG. 2. Left panel: average double occupation $\langle d \rangle_{av}$ on the honeycomb clusters with $L = 24$, 54, and 96 sites for different interaction strengths U/J in the local second Born, third-order, and T-matrix approximations, using the initial state (A). The black triangles correspond to exact data for the extended honeycomb lattice (taken from Ref. [42]). Right panel: time evolution of $\langle d \rangle_{av}$ for the local second Born calculations starting from the Hartree ground state [Eq. (11)], for which $\langle d \rangle_{av} = \langle d_i \rangle = \langle n_{i\uparrow} \rangle \langle n_{i\downarrow} \rangle = 0.25$.

spectral weight discussed below). Nevertheless, the excellent agreement with the reference data confirms the reliability of this procedure, which is computationally efficient as it requires comparatively few time steps.

Finally, the stationary values of the double occupations allow us to test the accuracy of the different approximations for the self-energy. The T-matrix result is accurate up to about $U/J = 1.5$ but for larger coupling starts to deviate from the reference. The third-order approximation and the local second Born result are very close to each other and work substantially better up to $U/J = 3.5$. Since the correlated states (A) and (B) are particle-hole symmetric, in an exact calculation, the third-order contributions to the self-energy would perfectly cancel each other [21,38,45]. Therefore, in the T-matrix approximation, the leading term beyond second order becomes unbalanced, which explains the poor performance in Fig. 2. For the same reason, both a full second Born calculation and a third-order simulation would be exact up to $\mathcal{O}(U^3)$, which also is the origin for the high accuracy of the local second Born results. These findings give us confidence to use the comparatively simple local second Born approximation for most simulations below [46].

Second, we study the photoemission spectrum, which is directly obtained from the less component $G^<_{ii\sigma}(t,t')$ of the nonequilibrium Green function (for details, see the Appendix). In Fig. 3, we present the photoemission signal $I_1(\omega)$ of the cluster with $L = 54$ sites recorded at the central site 1 (as labeled in Fig. 1). We show results for different values of U/J with a probe pulse arriving at some time after the transient regime (for the computational details and the specific probe pulse parameters, see Appendix A). In the case of half-filling, the Hartree approximation ($\Sigma = 0$) yields a photoemission signal with a few pronounced peaks which are independent of U/J. On the other hand, correlations lead to an essential broadening of the whole spectrum and, in particular, to single-particle energies beyond the cutoff energy $\omega_{cutoff} = -3J$ of the
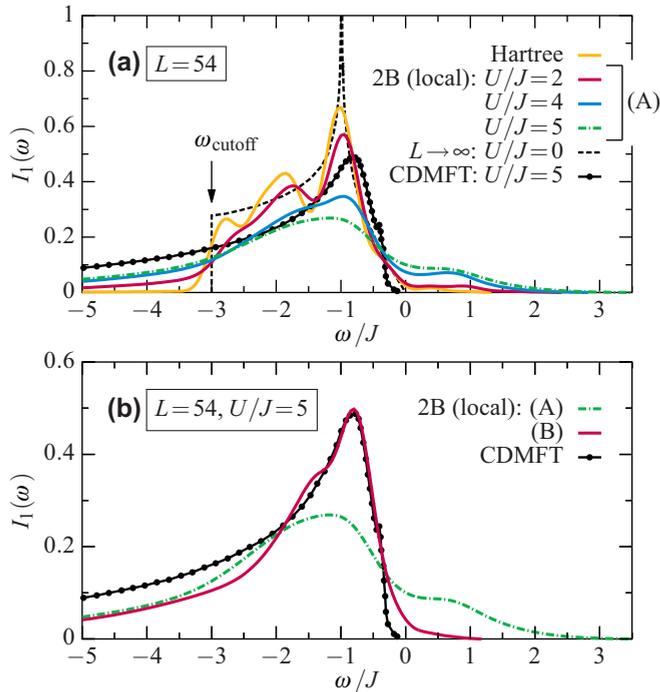
FIG. 3. (a) Photoemission signal $I_1(\omega)$ for the honeycomb cluster with $L = 54$ sites in Hartree approximation (U independent) and in local second Born approximation for different U/J, using the initial state (A) of Sec. II C. Black dashed line: spectrum of the extended lattice at $U/J = 0$ (e.g., Refs. [48,49]), black solid line: spectrum for $U/J = 5$, as obtained from a cluster-DMFT calculation [from Ref. [47] and also shown in panel (b)]. (b) Comparison of the photoemission signal $I_1(\omega)$ at $U/J = 5$ for local second Born calculations with different initial states. Green line: spectrum [as in panel (a)] for the initial state (A). Red line: correlated ground state (B).

noninteracting system (see the black dashed line and compare also with Fig. 11 in Appendix A). Moreover, this broadening is accompanied by a shift of the main peak (around $\omega = -J$) towards the Fermi energy, $\omega_F = 0$, as a function of the interaction strength. For $U/J = 5$ (green dashed-dotted line), we finally observe that the photoemission spectrum becomes rather flat due to enhanced occupations of single-particle energies above the Fermi level. These occupations originate from the fact that the equilibrated state is not the ground state of the system. On the contrary, if we first prepare the correlated ground state (B) (recall Sec. II C) and then propagate the nonequilibrium Green functions in time, we obtain a photoemission spectrum as shown by the red solid line in Fig. 3(b). If we compare it, for example, to a cluster-DMFT (CDMFT) study [47] for the extended honeycomb lattice (black solid line), we find a very good agreement. However, the finite spectral resolution introduced by the probe pulse does not allow us to recover the emergence of a small energy gap [48], which exists at finite onsite interactions U/J.

In summary, we conclude from Figs. 2 and 3 that already the local second Born approximation is able to capture important electron correlation properties of the honeycomb clusters. As the considered equilibrium properties are adequately described up to $U/J \approx 3\ldots4$, we will likewise analyze the stopping dynamics in Sec. IV up to this regime of interaction strengths.

IV. STOPPING DYNAMICS

A. Energy loss of the projectile

We now simulate collisions of protons ($Z_p = 1$) with honeycomb clusters of size $L = 24$ and 54. To characterize the stopping dynamics, we consider different impact kinetic energies $E_{\text{kin}} = \frac{1}{2}m_p\dot{\mathbf{r}}_p^2(t = 0)$, ranging from below 1 keV to about 0.5 MeV, and measure the energy loss S_e, defined as the change of the projectile's kinetic energy after passing through the lattice:

$$S_e = E_{\text{kin}}(t = 0) - E_{\text{kin}}(t \to \infty). \tag{13}$$

As function of $E_{\text{kin}}(t = 0)$, this quantity yields the energy loss spectrum, which is similar to the stopping power spectrum (spectrum of dissipated power per length) for the case of homogeneous media. Below, we specify the kinetic energy of the proton in units of keV/u, where u denotes the unified atomic mass unit.

We begin with the analysis of S_e for the smaller cluster [see Fig. 4(a)]. In Hartree approximation (black lines), we find a pronounced maximum of the energy loss in the regime of considered energies, which is the behavior known from the stopping power of nonrelativistic ions (we note, however, that the position of the maximum is typically at larger energies, compare with Sec. V). When U is increased, the peak height decreases and, at the same time, the peak slightly shifts towards larger proton energies. At large impact energies, the curves for different interaction strength approach each other, leading to a rather generic scaling of the energy loss as $\propto v_z^{-a}\ln(bv_z^2)$ (with fit parameters $a, b > 0$). Thus, the high-energy tail is consistent with predictions from the nonrelativistic Bethe formula [1]. On the other hand, for low energies, the change of the energy loss is closer to $\sim v_z$.

Next, we examine the influence of electron-electron correlations [cf. the red curves in Fig. 4(a)], which represent local second Born calculations for the initial state (A) of Sec. II C, where the lattice system has equilibrated before the impact of the proton. For small interactions $U/J \lesssim 2$, we find that corrections to the Hartree approximation are rather small. On the contrary, for $U/J = 4$, we observe clear deviations from the mean-field picture, with a decrease of S_e over a large energy window and a slight increase around $E_{\text{kin}} \approx 1$ keV/u.

In Fig. 4(b), we present the same analysis for the larger honeycomb cluster with $L = 54$ sites, including results for various approximations of the self-energy. While S_e becomes generally larger compared to the smaller cluster, we notice that correlations have the same effect of reducing the energy loss for proton energies of $E_{\text{kin}} \gtrsim 5$ keV/u, as was observed for $L = 24$. At the same time, the low-energy tail behaves differently: here we find a scaling $\propto \ln(v_z)$. Moreover, we observe that all considered self-energies lead to very similar stopping results. In particular, there is very good agreement between the local and full second-order Born approximation, which indicates that here it is sufficient to treat correlations locally. We emphasize again that a nonlocal self-energy (with $\Sigma_{ij} \neq 0$) or a more complex self-energy (including higher-order diagrams) generally brings about a drastic increase of the computation time, particularly on a large time grid, which is required to study the impact of slow projectiles. For this reason,
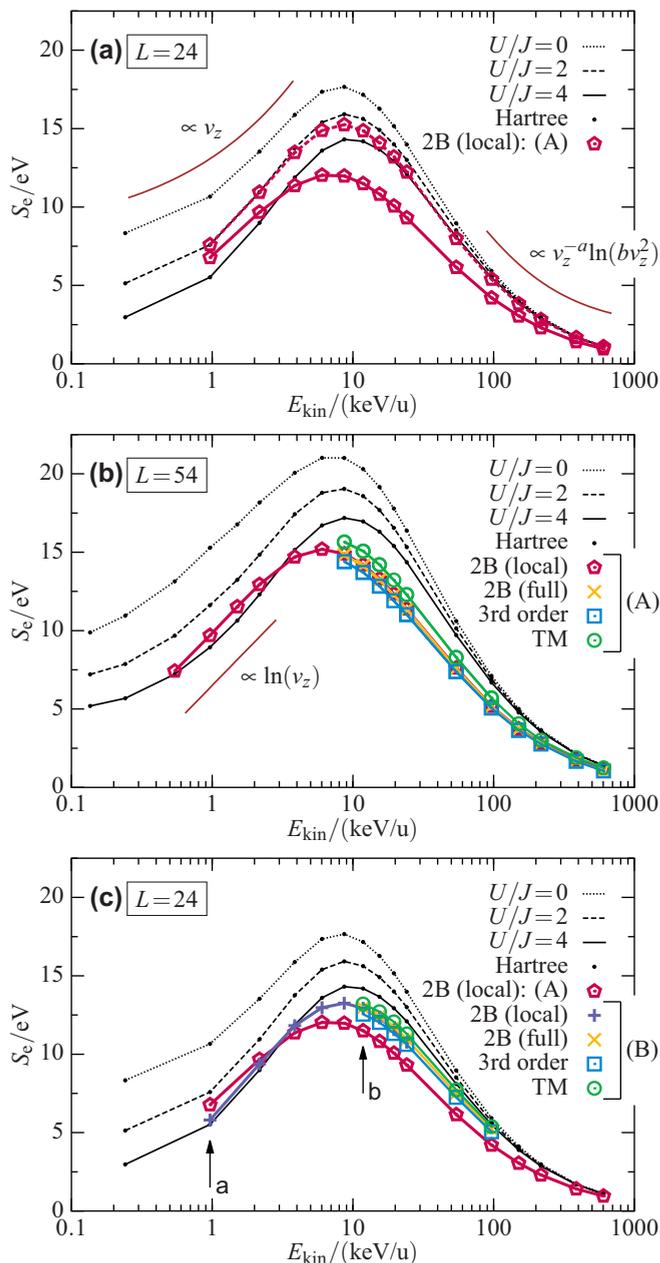
FIG. 4. Energy loss S_e for protons passing through honeycomb clusters of size $L = 24$ [panels (a) and (c)] and $L = 54$ [panel (b)]. In all panels, the value of the onsite interaction U/J is encoded in the line style, and the black lines indicate the results of the Hartree approximation. In panel (a), the red curves show the energy loss in the local second Born approximation with initial state (A). In panel (b), we present the same analysis for the larger cluster, including results of the full second Born (yellow), the third-order (blue), and the T-matrix approximation (green). Panel (c) shows the influence of initial correlations, comparing the second Born results of panel (a) to local and full second Born, third-order, as well as T-matrix calculations for the initial state (B). The arrows in panel (c) indicate the two situations analyzed in more detail in Fig. 5.

we show results beyond the local second Born approximation in Fig. 4(b) only for correspondingly large proton energies.

Standard stopping power calculations of a charged particle usually consider the target material in the ground state before

the collision. This is, however, not the case for our simulations with the initial condition (A) and self-energies beyond mean field. To quantify the effect of this systematic inconsistency, we repeat some of the simulations with the initial state (B) [see Fig. 4(c) for $L = 24$ and $U/J = 4$]. As a result, we observe that the form of the correlated initial state has a non-negligible influence on the energy loss of the projectile. In fact, we find that the self-consistent correlated ground state [case (B)] yields energy losses which are overall closer to those of the Hartree approximation. Nevertheless, there remain significant differences between correlated and mean-field calculations, most importantly around the maximum of the curves.

B. Time-dependent density response of the electron system

To gain insight into the effect of correlations on S_e and the physical mechanisms, we now analyze the response of the lattice electrons to the approaching projectile for a fixed value of the interaction strength $U/J = 4$. The general scenario is as follows. During the early stage of the dynamics, the electrons (initially distributed uniformly over the cluster with $\langle n_{i\sigma} \rangle = 0.5$) start to accumulate close to the impact point and, thus, create a negative net space charge, which attracts and accelerates the proton towards the cluster. After passing through the lattice plane, the proton then loses kinetic energy, depending on the nonadiabatic response of the electron density. For two different proton energies [indicated by arrows labeled a and b in Fig. 4(c)], the precise dynamics is shown in Fig. 5. There, we compare the Hartree approximation to the local second Born approximation for both considered initial states (A) and (B).

The difference in the time scale on which the observables change during the collision process is evident: While at a kinetic energy around 1 keV/u, the electron density and the double occupation in the center of the honeycomb cluster change on a time scale of a few inverse hopping times, $t_0 = \hbar/J$, they change on a time scale comparable to t_0 for the much faster proton ($\sim$10 keV/u). This difference has immediate consequences for the energy transfer to the lattice: From Fig. 5(b) (fast proton), we find that the exchange of energy between projectile and target occurs mainly during the stage of electron accumulation. Together with a retarded response of the electron density in the second Born approximation [dotted and solid lines in panel (b)], this translates into a faster proton (of a few eV) after the collision, as compared to the mean-field calculation (dashed line). On the contrary, for the slow proton, the energy loss is defined by both the buildup *and* the removal stage of the charge-induced confinement potential. For this reason it, is not *a priori* obvious how S_e is altered by correlations. This is also confirmed by the difference of the two second Born calculations [cf. in particular the center panel in Fig. 5(a)]. Here, the calculation which starts from the correlated ground state (dotted line) shows a density response rather close to the Hartree approximation [50], whereas the simulation which uses the equilibrated Hartree ground state as initial state (solid line) yields an energy transfer that is clearly larger than the mean-field result. The time evolution of the double occupation is, however, almost identical in both correlated cases, but significantly different from the mean-field approximation [see the bottom panel in Fig. 5(a)].
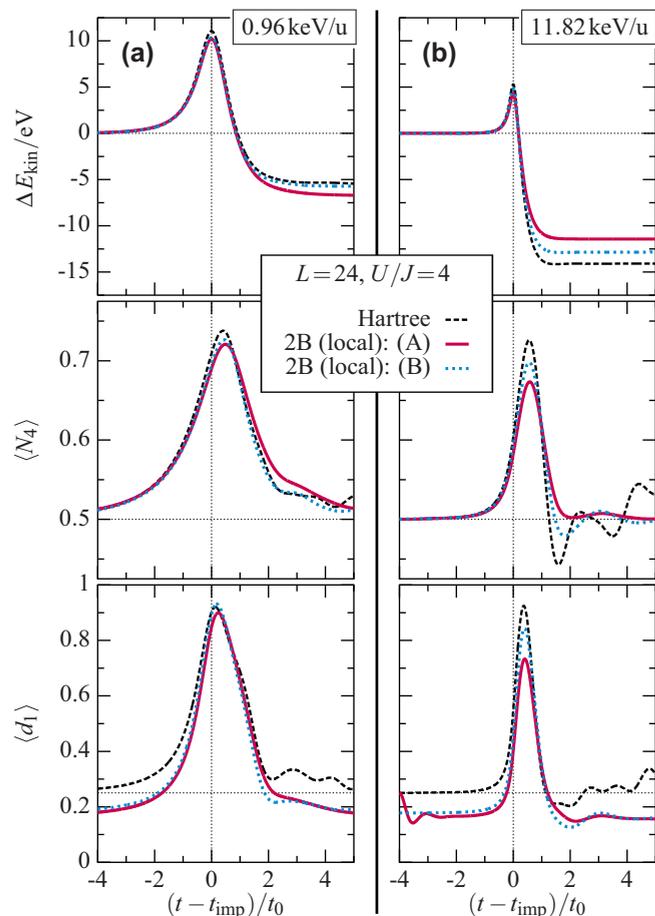
FIG. 5. Coupled proton-electron dynamics for the honeycomb cluster with $L = 24$ sites for two different proton energies, $E_{\mathrm{kin}} = 0.96$ keV/u (left panels) and 11.82 keV/u (right panels), corresponding to the arrows shown in Fig. 4(c). The coupling strength is fixed, $U/J = 4$, and three many-body approximations are compared (see inset). Top panels: change of the projectile's kinetic energy $\Delta E_{\mathrm{kin}}(t) = E_{\mathrm{kin}}(t) - E_{\mathrm{kin}}(t = 0)$ as function of time. Center panels: time evolution of the electron density averaged over the central sites labeled 1 to 4 in Fig. 1, i.e., $\langle N_4 \rangle(t) = \frac{1}{4} \sum_{i=1}^{4} \langle n_{i\sigma} \rangle(t)$. Bottom panels: time evolution of the double occupation $\langle d_1 \rangle(t) = \langle n_{1\uparrow} n_{1\downarrow} \rangle(t)$ on the site 1, which is closest to the impact point of the projectile.

C. Time-dependent electron spectral properties

An even closer look at the electronic excitations during the collision process is provided by the time-resolved photoemission spectrum $I(\omega, t_{\mathrm{p}}) = I_0^{-1} \sum_{i=1}^{L} I_i(\omega, t_{\mathrm{p}})$, with normalization factor I_0. Our NEGF approach directly yields this quantity (see Appendix), and we present the results in Fig. 6 for two different probe times t_{p}. Prior to the impact of the proton ($t_{\mathrm{p}} = 0$), the spectrum corresponds to the correlated ground state [we use initial state (B)] of the system and is, thus, analogous to the one discussed in Fig. 3(b). Note, however, that here we use $U/J = 4$, and we average over the whole cluster and use a different probe pulse. At a later time, when the projectile just passes the lattice plane ($t_{\mathrm{p}} \sim 4.1 t_0$), we observe a spectrum which indicates a strong redistribution of electrons in the lower Hubbard band, particularly towards lower energies
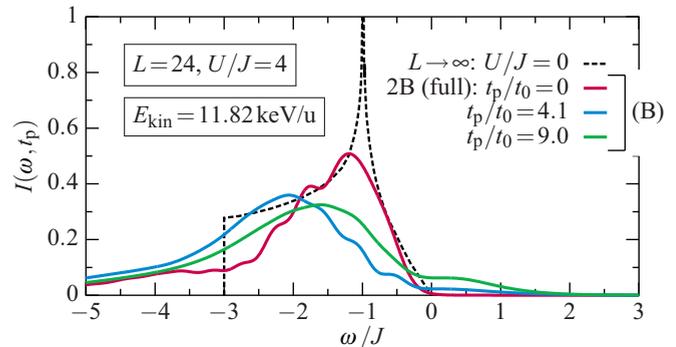
FIG. 6. Time-resolved photoemission spectrum $I(\omega, t_{\mathrm{p}}) = I_0^{-1} \sum_{i=1}^{L} I_i(\omega, t_{\mathrm{p}})$ of a cluster with $L = 24$ and $U/J = 4$ for the stopping dynamics of a proton with energy $E_{\mathrm{kin}} = 11.82$ keV/u [the scenario is similar to Fig. 5(b)]. The calculations are performed in full second Born approximation with a correlated initial state [case (B)]. Red curve: initial state, black dashes: ground state of an infinite system at $U/J = 0$. Blue line: spectrum when the projectile passes through the lattice plane. Green line: "final" state after the collision. To resolve the spectrum at the different stages of the dynamics, we have set the probe pulse width here to $\tau = 2 t_0$ (cf. Appendix A).

(blue line in Fig. 6). This redistribution is, obviously, a result of the negative electronic confinement potential induced to the lattice electrons by the projectile and corresponds to a net energy loss of the electron system. Finally, at time $t_{\mathrm{p}} \gtrsim 9 t_0$, the proton has passed through the lattice and is located far enough such that it does not affect the electrons anymore. We, therefore, measure a state of the electrons that is close to the "final" state. This state is characterized by a net energy gain of the electron system [as was shown in the top panel of Fig. 5(b)]. Here, we can resolve the spectral distribution of this energy: a substantial amount of electrons is being excited (above the Fermi level, $\omega_{\mathrm{F}} = 0$) into the upper Hubbard band. Of course, on a longer time scale (part of) this energy will be transferred from the electrons to lattice vibrations (phonons), but this is beyond the present model.

D. Projectile energy loss within the generalized Kadanoff-Baym ansatz

In this section, we analyze the generalized Kadanoff-Baym ansatz (GKBA) that was discussed in Sec. II C. This approximation has recently attracted growing attention [28,29,33,40] because it provides a way to significantly reduce the numerical effort of the computation of the NEGF, while still preserving the conservation laws of the chosen many-body approximations. Here, we apply the GKBA to reconstruct the two-time Green function $G_{ij\sigma}(t, t')$ for second Born self-energies from its time-diagonal value by using Hartree propagators (see Ref. [33] for details). For the present setup, the GKBA allows us to extend the full second Born calculations of Fig. 4(b) towards significantly longer times and, thus, to lower proton impact energies. We also note that, for finite systems which are strongly excited, the GKBA has been found to be free of certain artifacts of the two-time simulations [29], while being of comparable accuracy than the latter.
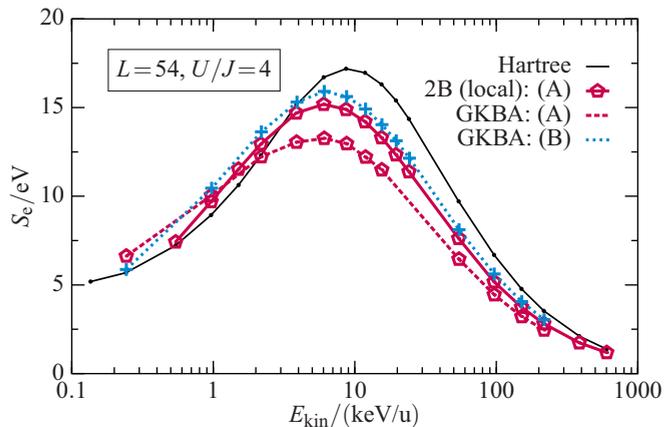
FIG. 7. Energy loss for the honeycomb cluster with $L = 54$ sites in second Born approximation. Comparison of the full two-time simulation and the GKBA (see text for details). Black and red solid lines are the same as in Fig. 4(b); red dashed and blue dotted curves: GKBA results for the initial states (A) and (B), respectively.

In Fig. 7, we present such GKBA simulations for both initial states, (A) and (B), as discussed above. For the initial state (A), we find a qualitative agreement with the analogous two-time calculations. At the same time, the GKBA simulations yield a systematically lower energy loss S_e for proton energies of $E_{kin} \gtrsim 5$ keV/u than the two-time simulations. In the present case, the projectile induces a rather strong and nonlocal perturbation, which is typically well described by the GKBA [29]. Whether the GKBA or two-time results for the stopping power are more accurate is presently unknown, as there are no exact results available, and this remains to be resolved in future studies.

Finally, we perform GKBA simulations with the fully correlated initial state (B). This leads to significantly increased results for the energy loss spectrum of the protons (blue dotted curve), which are closer to the mean-field result. The most striking achievement is that the GKBA simulations can be extended towards projectile energies around 200 eV. Interestingly, for these energies, the stopping power is significantly increased, as compared to the mean-field result. At the same time, with the use of Hartree propagators, we lose direct access to the correlated spectral functions.

E. Finite temperatures

For slow projectiles, we have seen in Secs. IV A and IV D that the inclusion of electron-electron correlations can lead to a slight increase of the energy loss in comparison to the mean-field treatment of the collision process. As this effect seems to be larger for a lattice system which is initially not in the self-consistent ground state [and thus has a nonzero effective temperature, cf. initial state (A)], it is worthwhile to discuss in more detail the influence of a finite electron temperature on the stopping dynamics.

In contrast to other approaches, the effect of finite temperature is straightforwardly incorporated in the NEGF formalism, where temperature effects enter the KBE via the initial state defined in Eq. (11). In Fig. 8, we perform Hartree and second Born calculations for $L = 24$ and different inverse
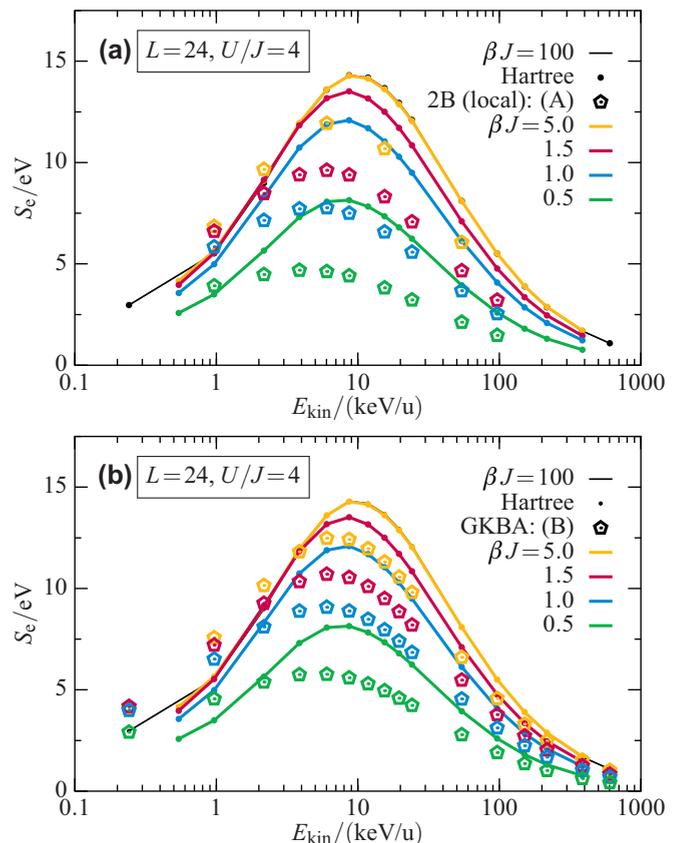
FIG. 8. Temperature dependence of the energy loss S_e for the honeycomb cluster with $L = 24$ sites and $U/J = 4$. Black lines: zero-temperature Hartree calculations, as in Fig. 4(a). Colored lines: Hartree results for different temperatures. Symbols: local second Born results for the same temperatures $\beta J = 5$, 1.5, 1, and 0.5. (a) Local second Born calculations with initial state (A). (b) GKBA calculations as in Sec. IV D with initial state (B).

temperatures $\beta J \ll 100$. For $\beta J = 5$, which corresponds to an electron temperature of $k_B T = 0.56$ eV (or about $T = 6500$ K) for a hopping amplitude of $J = 2.8$ eV, we measure energy loss spectra (cf. the yellow curves) that are still very close to the ground-state results of Fig. 4(a). For higher temperatures, $\beta J < 5$, on the other hand, we observe that the energy loss systematically decreases with temperature, whereas the maximum of the spectrum shifts to slightly lower energies. These trends continue even for higher electron temperatures (obviously, this refers to a nonequilibrium state, where the electron temperature is decoupled from the lattice) (see the red, blue, and green solid curves).

To understand the origin of the reduction of the energy loss with temperature, we investigate in Fig. 9 the time dependence of the proton energy and of the local electron density computed in mean-field approximation. Obviously, a temperature increase reduces the local enhancement of the electron density, as thermal fluctuations reduce the coherent response of the electrons to the projectile.

Finally, electron correlations are important even at the highest temperature considered [$\beta J = 0.5$ ($T \approx 65000$ K for $J = 2.8$ eV)], where the interaction energy U is still twice as large as the thermal energy. Here, compared to the mean-field
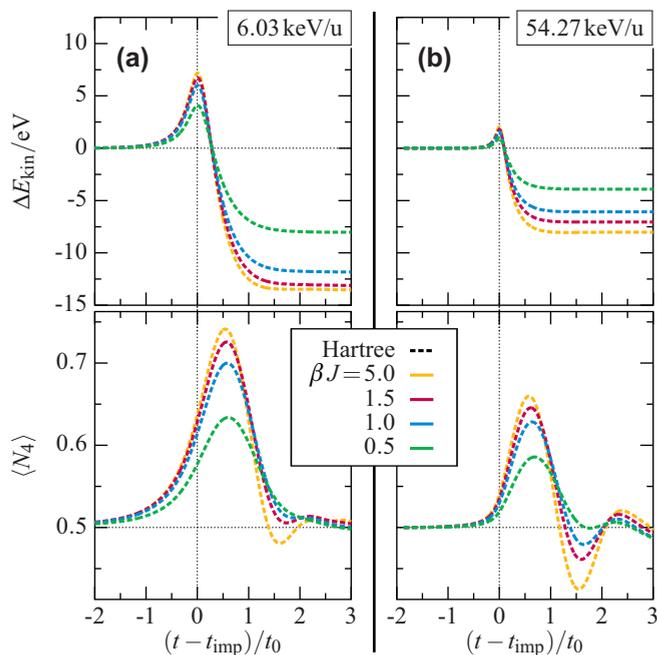
FIG. 9. Time-dependent energy change $\Delta E_{kin}(t) = E_{kin}(t) - E_{kin}(t = 0)$ of the proton (upper panels) and electron density $\langle N_4 \rangle(t) = \frac{1}{4}\sum_{i=1}^{4}\langle n_{i\sigma}\rangle(t)$ at the four sites around the impact point (lower panels) for different temperatures. Same cases (Hartree dynamics, $U/J = 4$) as shown in Fig. 8.

model, we observe that the local second Born calculations yield a clear shift of the whole spectrum towards smaller energies. Furthermore, the maximum energy loss is substantially reduced (with a peak value of the second Born calculation that is only about half of the mean-field result, Fig. 8(a)], which shows that the relative importance of correlations seems to increase with reduction of the temperature βJ. This unexpected behavior is due to the reduction of quantum diffraction effects with temperature, leading to an increased electron localization, which will be investigated in more detail elsewhere.

V. APPLICATION TO GRAPHENE

As a supplementary investigation, we examine, in this section, whether the coupled NEGF-Ehrenfest approach can be applied also to study the collision of charged particles with real (low-dimensional) materials. As example, we consider a two-dimensional sheet of graphene. As was shown in Refs. [51,52], the equilibrium properties of graphene [30,49] are well described through an extended Hubbard model with a nearest-neighbor hopping J on the honeycomb lattice using, beyond the onsite interaction U, additional nonlocal Coulomb interactions V_{ij}, that are known to stabilize the Dirac semimetallic phase [53]. However, it is not clear *a priori* whether this model holds also out of equilibrium. In particular, the present situation of the impact of a charged particle corresponds to a (locally) very strong excitation, driving the system far away from equilibrium. This question can only be answered by direct simulations of this process

and by comparison to reliable reference data for the stopping power.

In order to map this extended Hubbard model to the Hamiltonian of the form (1) with purely local interactions, we follow Ref. [31] and use an effective onsite interaction $U' = U - \bar{V} = 1.6J$, where $\bar{V}$ denotes a weighted average over the nonlocal contributions. Although this approximation has limitations, e.g. [52], it is agreed to be, at least, qualitatively correct. Moreover, we extend the Hamiltonian of Sec. II in two regards:

(i) We take into account the existence of four valence electrons per site. This means we consider (instead of a single-band model) a system with four independent Hubbard bands of equal hopping and interaction parameters, which together describe the dynamics of the four electrons provided by each sp^2-hybridized carbon atom in the graphene sheet. We are aware of the fact that such an approach excludes the specific nature of the σ and π bonds as well as possible (sp-)interband transitions. The main advantage of this model is, however, that it can be straightforwardly implemented by setting the local net charges Z_i in Eq. (3) to $Z_i = 4(1 - \sum_{\sigma}\langle n_{i\sigma}\rangle)$, leaving open a single parameter, the hopping amplitude J, which we will use below to adjust the maximum energy transfer.

(ii) We account for the fact that the incident projectile can influence the electron mobility on the lattice. This includes local changes to the electron's kinetic energy which originate from the presence of the off-diagonal matrix elements of the interaction potential W_{ij} between the projectile and the electrons on the lattice. Below, we approximate such a renormalization of the hopping to be proportional to the average potential energy between neighboring sites, i.e., we define an effective time- and site-dependent hopping amplitude

$$J_{ij}(t) = \begin{cases} -J + W_{ij}(t), & |i - j| = 1 \\ 0, & \text{otherwise} \end{cases} \quad (14)$$

where

$$W_{ij}(t) = \gamma \frac{W_{ii}(t) + W_{jj}(t)}{2}. \quad (15)$$

The proportionality factor γ can be interpreted as the strength of the orbital overlap and will be used as a second fit parameter below (see Appendix B for details).

We note that the ansatz (14) neglects corrections of the form W_{ij} with $|i - j| > 1$, which is justified because the wave functions of next-nearest and more distant neighbors have in general a much smaller overlap. Nevertheless, a further improved treatment of the off-diagonal components may be important for future studies since the projectile induces strong perturbations to the system.

In Fig. 10, we present stopping results for protons and alpha particles ($Z_p = 2$) for the model parameters $J = 3.15$ eV and $\gamma = 0.55$. To obtain reasonable agreement with *ab initio* TDDFT and SRIM data for the planar *infinitely extended* graphene sheet [7,8], we consider cluster sizes as large as $L = 384$, which are easily treated in Hartree approximation. The neglect of correlations is justified due to the relatively small onsite interaction strength of $U/J = 1.6$ (recall Sec. IV A). This expectation is confirmed by performing additional local second Born simulations for $L = 54$ (green circles) that lie on top of the Hartree curves [cf. Figs. 10(a) and 10(b)]. Generally,
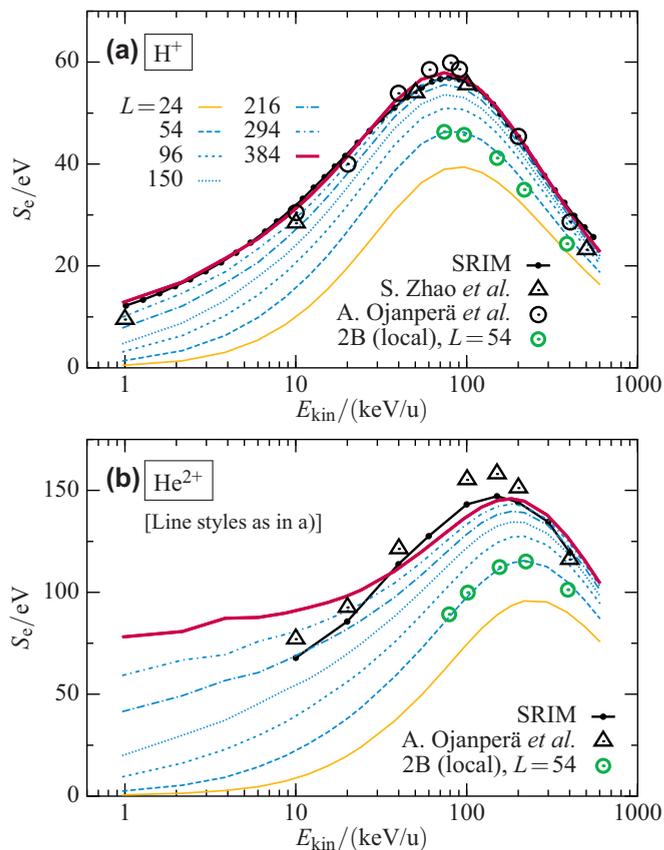
FIG. 10. Energy loss of (a) hydrogen ions (H$^+$) and (b) alpha particles (He^{2+}) penetrating through a single layer of graphene. In both panels, the strength of the Coulomb interaction is $U/J = 1.6$, the fit parameters are $J = 3.15$ eV and $\gamma = 0.55$, and the initial z position of the projectile is $z = 20a_0$. The Hartree results for different cluster sizes, ranging from $L = 24$ (bottom) to $L = 384$ (top), are shown by different line styles. For the cluster with $L = 54$ sites, we also performed second Born calculations (green circles) showing that correlation corrections are rather small in this case. For a detailed discussion of the U, J, and γ dependence, see Appendix B. The black symbols and lines correspond to *ab initio* TDDFT calculations and SRIM data, respectively (taken from Refs. [7,8]).

we find that the energy transfer increases with the cluster size, which is consistent with results for graphene clusters discussed in Ref. [9]. In Fig. 10(a), the curves $S_e(E_{kin})$ tend to converge for large L and, for practically all considered proton energies, well approach the energy loss given by the reference data.

Finally, an important test of the model is provided by Fig. 10(b). There, we use exactly the same model parameters J and γ to simulate the energy loss for collisions of single-layer graphene with bare helium nuclei (He^{2+}). Without further adjustments, we recover good agreement with the available reference data, including the increase of the overall magnitude of S_e compared to the case of protons and, in addition, the shift of the maximum energy loss towards larger kinetic energies.

Given the simplicity of the model Hamiltonian, it is interesting that our NEGF-based approach reveals the correct trends for a fairly realistic system. On the other hand, however, we have to note also problems of the model. In particular, at the low-energy tail of the energy loss curve, we observe

significantly larger values compared to the TDDFT simulation in the case of alpha particles [cf. the red curve in Fig. 10(b)]. The origin of these discrepancies is not fully clear yet, and, therefore, in this range, additional correlated simulations as well as improvements to the model are required in the future.

VI. CONCLUSIONS

In summary, we have presented a combined nonequilibrium Green functions and classical Ehrenfest dynamics approach to the interaction of a nonrelativistic charged particle with a (strongly) correlated system. Our approach allows for a fully time-dependent treatment and is, thus, able to resolve nonadiabatic processes in the electronic subsystems. To explore the role of electronic correlations, we performed solutions of the two-time Keldysh-Kadanoff-Baym equations using different many-body approximations for the self-energy: the second Born, third-order, and the T-matrix approximations. This enabled us to demonstrate that electron-electron correlations do significantly influence the slowing down of a charged projectile in, both, the low and high-energy limits. The high computational effort of the NEGF simulations has limited us to projectile energies of 1 keV, as lower impact energies increase the interaction time with the lattice and, in turn, the computing time. To extend the simulations to lower energies, we have applied the generalized Kadanoff-Baym ansatz (GKBA), which is substantially more efficient. Interestingly, these simulations predict an energy loss well above the mean-field model, indicating that correlations can enhance the slowing down of a (slow) projectile. How accurate these results are is not known at the moment. This requires further analysis via full two-time simulations, the use of improved self-energies such as T-matrix self-energies, as well as independent TDDFT simulations.

Of particular current interest is the energy loss of low-energy (below 1 keV) charged particles in solid materials. An important field of applications are low-temperature plasmas. Questions of interest include the stopping power in materials with very strong electronic correlations (e.g., lattice models with $U/J \gtrsim 10$) or for magnetically ordered systems or insulators, where the stopping power can vanish below a certain threshold [54]. Furthermore, it will be important to extend the model beyond the Hubbard model to better capture realistic material properties, e.g., by using a Kohn-Sham basis. This, however, will drastically increase the computational requirements.

Additional questions of interest at low energies concern the inclusion of all relevant dissipation mechanisms, in particular, inelastic mechanisms such as phonons, impact excitation, and ionization or reemission of particles. Further relevant processes include neutralization of the ion before impact and capture (sticking), which is expected to cause deviations from the linear velocity scaling. Finally, it will be important to also consider more complex charged projectiles that are different from bare ionic cores. Here, intraionic electronic excitations play an important role in the stopping dynamics, e.g., [55].

From a technological point of view, it would furthermore be interesting to explore whether the energy deposition can be externally controlled, e.g., by time-dependent (laser) fields, which excite the target material before or during the impact. The potential effect of such an out-of-equilibrium situation

was demonstrated by an analysis of an increased temperature of the electronic subsystem. For such kinds of nonequilibrium investigations, our NEGF-based approach represents an optimal toolbox, as it handles external fields self-consistently and nonperturbatively and can include arbitrary scattering processes in a systematic way.

APPENDIX A: TIME-RESOLVED PHOTOEMISSION SPECTRUM

As an essential test for the numerics and the time propagation of the KBE (7), we verify here whether the correct spectrum and bandwidth are recovered from the two-time NEGF in the limit of an infinite honeycomb lattice. To this end, we compute the photoemission spectrum for vanishing onsite interaction [$U = 0$ in Hamiltonian (1)] and consider clusters of different size L.

We consider the photoemission signal of a reference site i, which is given by [56]

$$I_i(\omega, t_{\mathrm{p}}) = -i \int dt \int dt'\, s(t - t_{\mathrm{p}}) s(t' - t_{\mathrm{p}}) e^{i\omega(t-t')} G_{ii\sigma}^<(t, t') \tag{A1}$$

at some probe time t_{p}. The function $s(t)$ thereby describes the envelope of the probe pulse and is chosen to be of Gaussian form, i.e.,

$$s(t) = \frac{1}{\tau\sqrt{2\pi}} e^{-t^2/(2\tau^2)}, \tag{A2}$$

where we set $\tau = 4t_0$ with $t_0 = \hbar/J$ and $J = 2.8$ eV.

Figure 11 shows the spectrum $I_1(\omega)$ for honeycomb clusters with up to $L = 216$ sites at a probe time $t_{\mathrm{p}} = 8t_0$, where, to evaluate the integral in Eq. (A1), we have computed the nonequilibrium Green function up to $t, t' = 15t_0$. Aside from some pulse-induced peak broadening, we observe that the
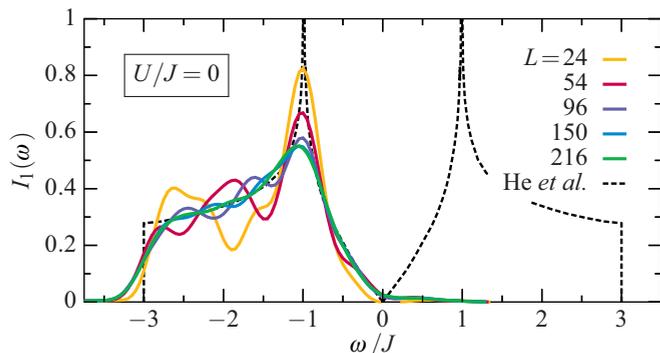
smaller clusters reveal only a few single-particle states, which are due to the finite system size. On the other hand, the spectra of the larger clusters ($L > 96$ sites) approach already well the density of states in the lower (valence) band of the extended honeycomb lattice (cf. the black dashed line).

APPENDIX B: ADAPTATION OF THE MODEL TO GRAPHENE

In order to model the impact of protons on a single sheet of graphene, we have tuned in Sec. V the hopping amplitude J and the orbital overlap parameter γ [defined in Eq. (14)] such that the energy loss spectrum is in good agreement with first-principles and SRIM data. By performing Hartree calculations, we show in Fig. 12 in more detail how the energy transfer S_e varies when these parameters are changed. Moreover, we discuss the influence of the ratio of the onsite Coulomb interaction U to the hopping J.

From Fig. 12(a), we observe that the interaction strength mainly influences the energy transfer below about 20 keV/u, whereas the high-energy tail remains unchanged. In the course of this, the low-energy tail as well as the maximum energy loss increase fairly linearly with U/J. Figure 12(b) shows that the hopping amplitude and the overlap parameter γ
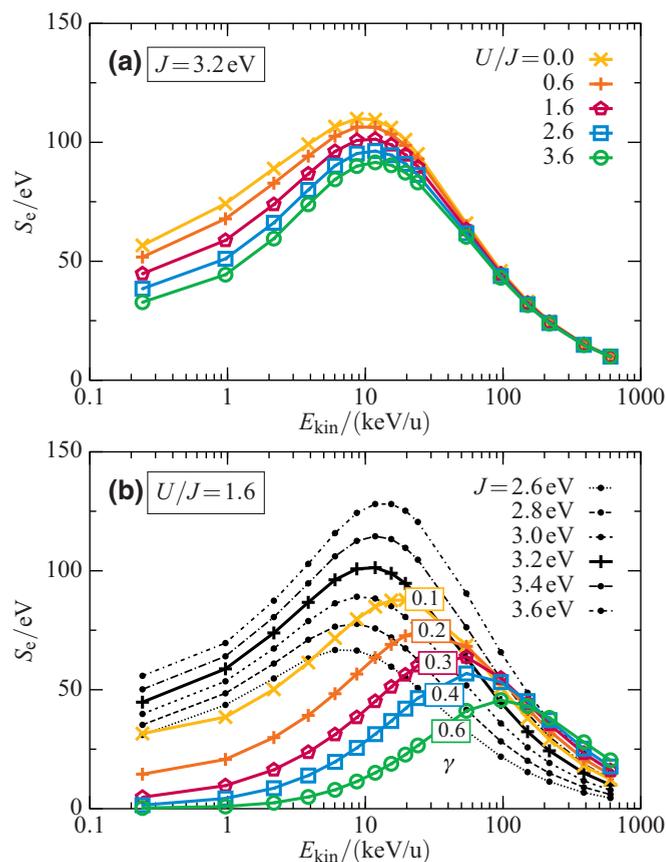
FIG. 12. Proton stopping dynamics as in Sec. V, but for different parameters U, J, and γ in Hartree approximation. The system size is $L = 54$. (a) Influence of the onsite interaction U for fixed $J = 3.2$ eV and $\gamma = 0$. (b) Influence of the hopping amplitude J and the orbital overlap γ for fixed interaction strength of $U/J = 1.6$.

FIG. 11. Photoemission spectrum $I_1(\omega)$ for different uncorrelated honeycomb clusters of size L, measured at a probe time $t_{\mathrm{p}} = 8t_0$ with $\tau/t_0 = 4$ [cf. Eq. (A1)]. The black dashed line shows the density of states in the valence and conduction band of the extended honeycomb lattice at half-filling, e.g., Refs. [48,49].

affect the energy transfer substantially more than the Coulomb interaction. For a fixed value $U/J = 1.6$, a larger value of J (i.e., an increase of the general electron mobility on the lattice) leads to a larger energy loss, independently of the initial kinetic energy of the projectile. On the other hand, if we increase the hopping locally by choosing $\gamma > 0$, we find that the energy transfer becomes considerably smaller, which is accompanied by a shift of the maximum of S_e towards larger kinetic energies.

[1] P. Sigmund, *Particle Penetration and Radiation Effects* (Springer, Berlin, 2006).

[2] I. Nagy and B. Apagyi, Phys. Rev. A **58**, R1653(R) (1998).

[3] J. M. Pitarke, R. H. Ritchie, and P. M. Echenique, Phys. Rev. B **52**, 13883 (1995).

[4] M. Quijada, A. G. Borisov, I. Nagy, R. Díez Muiño, and P. M. Echenique, Phys. Rev. A **75**, 042902 (2007).

[5] M. A. Zeb, J. Kohanoff, D. Sánchez-Portal, A. Arnau, J. I. Juaristi, and E. Artacho, Phys. Rev. Lett. **108**, 225504 (2012).

[6] A. Schleife, Y. Kanai, and A. A. Correa, Phys. Rev. B **91**, 014306 (2015).

[7] S. Zhao, W. Kang, J. Xue, X. Zhang, and P. Zhang, J. Phys.: Condens. Matter **27**, 025401 (2015).

[8] A. Ojanperä, A. V. Krasheninnikov, and M. Puska, Phys. Rev. B **89**, 035120 (2014).

[9] S. Bubin, B. Wang, S. Pantelides, and K. Varga, Phys. Rev. B **85**, 235435 (2012).

[10] F. Mao, C. Zhang, C.-Z. Gao, J. Dai, and F.-S. Zhang, J. Phys.: Condens. Matter **26**, 085402 (2014).

[11] R. Ullah, F. Corsetti, D. Sánchez-Portal, and E. Artacho, Phys. Rev. B **91**, 125203 (2015).

[12] M. A. Zeb, J. Kohanoff, D. Sánchez-Portal, and E. Artacho, Nucl. Instrum. Methods Phys. Res., Sect. B **303**, 59 (2013).

[13] J. M. Pruneda, D. Sánchez-Portal, A. Arnau, J. I. Juaristi, and E. Artacho, Phys. Rev. Lett. **99**, 235501 (2007).

[14] J. F. Ziegler, M. D. Ziegler, and J. P. Biersack, Nucl. Instrum. Meth. B **268**, 1818 (2010); J. F. Ziegler, J. P. Biersack, and U. Littmark, *The Stopping and Range of Ions in Solids* (Pergamon, New York, 1985).

[15] V. U. Nazarov, J. M. Pitarke, C. S. Kim, and Y. Takada, Phys. Rev. B **71**, 121106(R) (2005).

[16] V. U. Nazarov, J. M. Pitarke, Y. Takada, G. Vignale, and Y.-C. Chang, Phys. Rev. B **76**, 205103 (2007).

[17] V. I. Anisimov, F. Aryasetiawan, and A. I. Lichtenstein, J. Phys.: Condens. Matter **9**, 767 (1997).

[18] R. Singla, G. Cotugno, S. Kaiser, M. Först, M. Mitrano, H. Y. Liu, A. Cartella, C. Manzoni, H. Okamoto, T. Hasegawa, S. R. Clark, D. Jaksch, and A. Cavalleri, Phys. Rev. Lett. **115**, 187401 (2015).

[19] L. P. Kadanoff and G. Baym, *Quantum Statistical Mechanics* (W. A. Benjamin, New York, 1962).

[20] G. Stefanucci and R. van Leeuwen, *Nonequilibrium Many-Body Theory of Quantum Systems: A Modern Introduction* (Cambridge University Press, Cambridge, 2013).

[21] N. Schlünzen, S. Hermanns, M. Bonitz, and C. Verdozzi, Phys. Rev. B **93**, 035107 (2016).

[22] N. E. Dahlen and R. van Leeuwen, Phys. Rev. Lett. **98**, 153004 (2007).

[23] A. Stan, N. E. Dahlen, and R. van Leeuwen, J. Chem. Phys. **130**, 224101 (2009).

[24] K. Balzer, S. Bauch, and M. Bonitz, Phys. Rev. A **81**, 022510 (2010).

[25] K. Balzer, S. Bauch, and M. Bonitz, Phys. Rev. A **82**, 033427 (2010).

[26] M. Garny and M. M. Müller, *High Performance Computing in Science and Engineering, Garching/Munich 2009* (Springer, Berlin, 2010).

[27] K. Balzer and M. Bonitz, Lect. Notes Phys. **867** (2013).

[28] S. Latini, E. Perfetto, A.-M. Uimonen, R. van Leeuwen, and G. Stefanucci, Phys. Rev. B **89**, 075306 (2014).

[29] S. Hermanns, N. Schlünzen, and M. Bonitz, Phys. Rev. B **90**, 125111 (2014).

[30] M. I. Katsnelson, *Graphene: Carbon in Two Dimensions* (Cambridge University Press, Cambridge, 2012).

[31] M. Schüler, M. Rösner, T. O. Wehling, A. I. Lichtenstein, and M. I. Katsnelson, Phys. Rev. Lett. **111**, 036601 (2013).

[32] L. V. Keldysh, Zh. Eksp. Teor. Fiz. **47**, 1515 (1964) [Sov. Phys.–JETP **20**, 1018 (1965)].

[33] N. Schlünzen and M. Bonitz, Contrib. Plasma Phys. **56**, 5 (2016).

[34] K. Balzer and M. Eckstein, Phys. Rev. B **89**, 035148 (2014).

[35] K. Balzer, J. Phys.: Conf. Ser. **696**, 012001 (2016).

[36] C. Gramsch and M. Potthoff, Phys. Rev. B **92**, 235135 (2015).

[37] M. Puig von Friesen, C. Verdozzi, and C.-O. Almbladh, Phys. Rev. Lett. **103**, 176404 (2009).

[38] S. Hermanns, Ph.D. dissertation, Kiel University, 2016.

[39] P. Lipavský, V. Špička, and B. Velický, Phys. Rev. B **34**, 6933 (1986).

[40] E. Perfetto, A.-M. Uimonen, R. van Leeuwen, and G. Stefanucci, Phys. Rev. A **92**, 033419 (2015).

[41] A. Rios, B. Barker, M. Buchler, and P. Danielewicz, Ann. Phys. **326**, 1274 (2011).

[42] S. Sorella and E. Tosatti, Europhys. Lett. **19**, 699 (1992).

[43] M. Bonitz and D. Kremp, Phys. Lett. A **212**, 83 (1996).

[44] D. Semkat, D. Kremp, and M. Bonitz, Phys. Rev. E **59**, 1557 (1999).

[45] F. Gebhard, E. Jeckelmann, S. Mahlert, S. Nishimoto, and R. M. Noack, Eur. Phys. J. B **36**, 491 (2003).

[46] We note that in the case of an external excitation (as the field of a charged projectile) the particle-hole symmetry breaks and the second Born self-energy becomes $\mathcal{O}(U^2)$. Nevertheless, the Hubbard sites remain predominantly half-filled which makes the error in $\mathcal{O}(U^3)$ small.

[47] A. Liebsch, Phys. Rev. B **83**, 035113 (2011).

[48] R.-Q. He and Z.-Y. Lu, Phys. Rev. B **86**, 045105 (2012).

[49] A. H. C. Neto, F. Guinea, N. M. R. Peres, K. S. Novoselov, and A. K. Geim, Rev. Mod. Phys. **81**, 109 (2009).

[50] We note that the density matrix $\langle \rho_{ij\sigma} \rangle$ of the correlated ground state [e.g., in the local second Born approximation, case (B)] is more similar to that of the Hartree ground state than to that of the equilibrated Hartree ground state [case (A)].

[51] T. O. Wehling, E. Şaşıoğlu, C. Friedrich, A. I. Lichtenstein, M. I. Katsnelson, and S. Blügel, Phys. Rev. Lett. **106**, 236805 (2011).

[52] H.-K. Tang, E. Laksono, J. N. B. Rodrigues, P. Sengupta, F. F. Assaad, and S. Adam, Phys. Rev. Lett. **115**, 186602 (2015).

[53] W. Wu and A.-M. S. Tremblay, Phys. Rev. B **89**, 205128 (2014).

[54] S. N. Markin, D. Primetzhofer, and P. Bauer, Phys. Rev. Lett. **103**, 113201 (2009).

[55] M. Pamperin, F. X. Bronold, and H. Fehske, Phys. Rev. B **91**, 035440 (2015).

[56] M. Eckstein and M. Kollar, Phys. Rev. B **78**, 245113 (2008).